Journal of Solid State Chemistry 183 (2010) 2329–2342

Contents lists available at ScienceDirect

Journal of Solid State Chemistry

journal homepage: www.elsevier.com/locate/jssc

Crystal structure and physical properties of quaternary clathrates $Ba_8Zn_xGe_{46-x-y}Si_y$, $Ba_8(Zn,Cu)_xGe_{46-x}$ and $Ba_8(Zn,Pd)_xGe_{46-x}$

Navida Nasir [a], Andriy Grytsiv [a], Nataliya Melnychenko-Koblyuk [a], Peter Rogl [a,*], Ingeborg Bednar [b], Ernst Bauer [b]

[a] Institute of Physical Chemistry, University of Vienna, A-1090 Wien, Austria
[b] Institute of Solid State Physics, Vienna University of Technology, A-1040 Wien, Austria

ARTICLE INFO

Article history:
Received 25 May 2010
Received in revised form
29 July 2010
Accepted 31 July 2010
Available online 6 August 2010

Keywords:
Quaternary systems
Clathrate type I
Crystal structure
Phase equilibria
Physical properties

ABSTRACT

Three series of vacancy-free quaternary clathrates of type I, $Ba_8Zn_xGe_{46-x-y}Si_y$, $Ba_8(Zn,Cu)_xGe_{46-x}$, and $Ba_8(Zn,Pd)_xGe_{46-x}$, have been prepared by reactions of elemental ingots in vacuum sealed quartz at 800 °C. In all cases cubic primitive symmetry (space group $Pm\bar{3}n$, $a\sim1.1$ nm) was confirmed for the clathrate phase by X-ray powder diffraction and X-ray single crystal analyses. The lattice parameters show a linear increase with increase in Ge for $Ba_8Zn_xGe_{46-x-y}Si_y$. *M* atoms (Zn, Pd, Cu) preferably occupy the 6*d* site in random mixtures. No defects were observed for the 6*d* site. Site preference of Ge and Si in $Ba_8Zn_xGe_{46-x-y}Si_y$ has been elucidated from X-ray refinement: Ge atoms linearly substitute Si in the 24*k* site whilst a significant deviation from linearity is observed for occupation of the 16*i* site. A connectivity scheme for the phase equilibria in the "Ba_8Ge_{46}" corner at 800 °C has been derived and a three-dimensional isothermal section at 800 °C is presented for the Ba–Pd–Zn–Ge system. Studies of transport properties carried out for $Ba_8\{Cu,Pd,Zn\}_xGe_{46-x}$ and $Ba_8Zn_xSi_yGe_{46-x-y}$ evidenced predominantly electrons as charge carriers and the closeness of the systems to a metal-to-insulator transition, fine-tuned by substitution and mechanical processing of starting material Ba_8Ge_{43}. A promising figure of merit, *ZT* ~0.45 at 750 K, has been derived for $Ba_8Zn_{7.4}Ge_{19.8}Si_{18.8}$, where pricey germanium is exchanged by reasonably cheap silicon.

1. Introduction

Semiconducting compounds with clatharate-type I structure continue to be of considerable attraction for thermoelectric application. The structure of the typical type I clathrate consists of a framework of Si- or Ge-atoms forming two different types of polyhedral cages each of which can host a large guest atom. The possibility of substitution at guest atoms sites and/or framework atom sites can fine-tune electronic and thermal transport properties of the material. Our recent research has been devoted to Ba-, Ge- and Si-based clathrate systems such as $Ba_8M_x\{Si,Ge\}_{46-x-y}\square_y$ (M=Mn, Fe, Co, Zn, Cd, Pd, Pt, Cu; $\square$=vacancy) where detailed structural analyses and phase equilibria have been studied [1–6]. Substitution of *M* in Ge-based clathrates was shown to reduce the concentration of vacancies in parent binary $Ba_8Ge_{43}\square_3$ [7]. For Si-based clathrates, transition metal *M* atoms can act as a stabilizer for a ternary clathrate compound as binary $Ba_{8-\delta}Si_{46}$ is stable only above ~3 GPa [8]. It was demonstrated that substitution of *M*-atoms drives the metallic system towards metal-to-insulator transition, giving rise to interesting thermoelectric properties [1–5]. It was further established that *M* atoms preferentially occupy the 6*d* site, which for low *M*-contents is also associated with vacancies in Ge-based clathrates [1,2,4].

Although research has concentrated on the substitution of Group III and transition metal elements for Group IV atoms (Si, Ge) still little has been done to study the effect of substitution of Si for Ge. Superconductivity and crystal structure of the solid solutions $Ba_{8-\delta}Si_{46-x}Ge_x$ ($0\le x\le 23$) have been reported in Ref. [8]. Cage size control of guest vibrations and thermal conductivity was studied in $Sr_8Ga_{16}Si_{30-x}Ge_x$ [9]. Structural and transport properties of $Ba_8Ga_{16}Si_xGe_{30-x}$ were investigated in Ref. [10], whereas Nenghabi and Myles [11] have recently studied the structural and electronic properties of $Ba_8Ga_{16}Si_xGe_{30-x}$ and $Sr_8Ga_{16}Si_{30-x}Ge_x$ for x=0, 5, 15.

Although $Ba_8Ga_{16}Ge_{30}$ was shown to exhibit a figure of merit ZT=1.4 at 600 °C [12], the rather high costs for Ga and Ge exclude any technical application at large scale. But low price elemental combinations for clathrates have so far suffered from insufficiently high thermoelectric efficiency for TEG-applications in for instance automotive exhaust systems. In order to improve the thermoelectric figure of merit *ZT*, we pursue two options simultaneously: (a) electron band structure engineering by introduction of elements with significant electron DOS at the Fermi level (for instance Pd

* Corresponding author.
E-mail address: peter.franz.rogl@univie.ac.at (P. Rogl).

0022-4596/$ - see front matter © 2010 Elsevier Inc. All rights reserved.
doi:10.1016/j.jssc.2010.07.047

(see DOS calculation by Johnsen et al. [13]) and (b) phonon engineering to reduce lattice thermal conductivity via introduction of additional scattering of heat carrying phonons on lattice defects (i.e., random substitution-disorder, etc.) and nanostructuring grain size in nanostructured bulk material. Thus the present work therefore attempts to synthesize vacancy free type I quaternary clathrate phases and to elucidate their thermoelectric performance. For this task it will be necessary to evaluate structural details and phase relations for (i) partial substitution of Zn by Pd or Cu in clathrate $Ba_8Zn_xGe_{46-x}$ ($6<x<7.7$) and (ii) substitution of Ge for Si in the solid solution $Ba_8Zn_xGe_{46-x-y}Si_y$ ($7<x<7.7$).

Our previous and detailed studies on clathrate systems revealed that there is no vacancy in the 6*d* site for $x_{Zn}\geq 6$ in $Ba_8Zn_xGe_{46-x}$ [1], for $x_{Pd}\geq 3.8$ in $Ba_8Pd_xGe_{46-x}$ [2], and for $x_{Cu}\geq 5.3$ atoms in $Ba_8Cu_xGe_{46-x}$ clathrates [4]. For all these values the ternary solid solutions approach a semiconducting behavior. Therefore, the *M* to Ge ratio was maintained at 6:40 for all quaternary alloys and only the clathrate solid solutions with $x_{(M+Zn)}\geq 6$ were prepared and investigated. Moreover, the germanium-based clathrate system $Ba_8Zn_xGe_{46-x}$ reveals a continuous solid solution deriving from binary $Ba_8Ge_{43}\square_3$ with three framework defects in the 6*d* site [1,7], $Ba_8Zn_7Si_{39}$ clathrates have no binary counterpart $Ba_8Si_{46-x}\square_x$ ($Ba_{8-\delta}Si_{46-x}\square_x$ is not stable at 800 °C under normal pressure [8,14] and was said to exhibit defects at the 2*a* site occupied by Ba [8]). Consequently, there is only a very small homogeneity range in the ternary clathrate $BaZn_xSi_{46-x}$ around $x\sim 7$; however, no defects were encountered for Ba in site 2*a* [5]. In order to provide a semiconducting framework in the quarternary clathrate solid solution $Ba_8Zn_xGe_ySi_{46-x-y}$, Zn contents were always maintained ≥ 7.

2. Experimental

Alloys with a weight of 2–4 g for all quaternary systems, Ba–Pd–Zn–Ge, Ba–Cu–Zn–Ge, and Ba–Zn–Si–Ge, were prepared in two steps. In the first step master alloys $Ba_8M_xGe_{46-x}$ (*M*=Cu, Pd) and $Ba_8Ge_xSi_{46-x}$ were prepared by argon arc melting from elemental ingots (purity better than 99.9 wt%) on a water cooled copper hearth. In the second step the proper amount of Zn according to stoichiometry was added to each master alloy and vacuum-sealed in quartz tubes. Reactions were carried out at 800 °C for 4 days followed by quenching in cold water. Afterwards the reaction products were powdered to a particle size below 100 μm. Samples for physical property measurement were compacted in cylinders with diameter 10 mm and height 6 mm by hot pressing in a graphite die at 800 °C (argon atmosphere, pressure 60 MPa, FCT hot press system HP W 200/250 2200-200-KS). The cylindrical specimens were then annealed in vacuum-sealed quartz tubes at $T=800$ °C for 2–4 days followed by quenching in cold water.

In order to see the influence of the grain size on the physical properties, one sample with nominal composition $Ba_8Zn_8Ge_{19}Si_{19}$ was ball-milled to a grain size well below 1 μm (Fritsch Vario-Planetary mill Pulverisette 4 with tungsten carbide (WC) walled container and WC-balls) and hot pressed.

Details of the various techniques of characterization of compositions via light optical and scanning electron microscopy (SEM, EPMA on a Carl Zeiss DSM 962 equipped with a Link EDX system operated at 20 kV and 60 μA and Carl Zeiss EVO 40 equipped with a Pentafet Link EDX system; binary Ba_8Ge_{43}, Ba_6Ge_{25} and ternary $Ba_8Zn_{7.7}Ge_{38.3}$ clathrates were used as internal standards), of crystal structure (X-ray powder (XRP) and single crystal (XRSC) diffraction on single crystals $Ba_8Pd_3Zn_3Ge_{40}$ and $Ba_8Cu_3Zn_3Ge_{40}$) and of physical properties, which comprise electronic and thermal transport have been described in our previous papers [1,2].

The uncertainty of the measurement for the electrical resistivity is 2% and for the Seebeck coefficient is about 3–4%. The thermal conductivity was calculated from the thermal diffusivity D_t measured by a laser flash method (Flashline-3000, ANTER, USA), specific heat C_p and density ρ_d using the relationship $\kappa=D_tC_p\rho_d$. The errors of the measurement for the thermal conductivity is $<5\%$ in the range 100–400 °C. The density was measured by the Archimedes method in distilled water using a Mettler AE200 balance and agrees within 0.1–1.2% with the density determined by the direct volume method.

3. Results and discussion

3.1. Crystal structure of $Ba_8M_xZn_yGe_{46-x-y}$ (M=Pd, Cu)

In order to evaluate atom site preference in both solid solutions $Ba_8Pd_xZn_yGe_{46-x-y}$ ($x=1$, 2, 2.25, 2.4; $y=3.3$, 3.75, 4, 5) and $Ba_8Cu_xZn_{6-x}Ge_{40}$ ($x=2$, 3, 4, 5.2, 5.25, 5.5, 5.75), X-ray powder profiles were collected at room temperature from single-phase

Table 1
Composition from EMPA and crystallographic data for $Ba_8Pd_xZn_yGe_{46-x-y}$ and $Ba_8Cu_xZn_yGe_{46-x-y}$ alloys.

Nominal composition	EMPA (±1.0 at%)				Accepted composition	Lattice parameter *a*, nm	Ge2 in 16*i* (*x*, *x*, *x*)	Ge3 in 24*k* (0, *y*, *z*)	
	Ba	M	Zn	Ge				*y*	*z*
$Ba_8Pd_3Zn_3Ge_{40}$	14.9	4.5	6.1	74.6	$Ba_8Pd_{2.4}Zn_{3.3}Ge_{40.3}$	1.07683(1)	0.18266(5)	0.11931(8)	0.31137(8)
					$Ba_8Pd_{2.4}Zn_{3.3}Ge_{40.3}$[a]	1.07709(2)	0.18327(3)	0.11859(4)	0.31115(4)
$Ba_8Pd_2Zn_4Ge_{40}$	15.1	2.9	8.3	73.8	$Ba_8Pd_{1.5}Zn_{4.4}Ge_{40.1}$	1.07680(2)	0.1833(1)	0.1184(2)	0.3112(2)
$Ba_8Pd_{2.25}Zn_{3.75}Ge_{40}$	15.0	2.4	8.5	74.1	$Ba_8Pd_{1.3}Zn_{4.5}Ge_{40.2}$	1.07618(1)	0.1827(12	0.1190(2)	0.3105(2)
$Ba_8PdZn_5Ge_{40}$	15.0	1.7	9.6	73.7	$Ba_8Pd_{0.9}Zn_{5.1}Ge_{40.0}$	1.07631(2)	0.18270(5)	0.11823(7)	0.31024(7)
$Ba_8PdZn_5Ge_{40}$	15.1	1.3	10.7	72.9	$Ba_8Pd_{0.7}Zn_{5.7}Ge_{39.6}$	1.07632(2)	0.18335(7)	0.1175(1)	0.3103(1)
$Ba_8Pd_2Zn_7Ge_{37}$	14.9	1.3	11.0	72.7	$Ba_8Pd_{0.7}Zn_{5.9}Ge_{39.4}$	1.07643(1)	0.18305(9)	0.1181(1)	0.3105(1)
$Ba_8Pd_{2.4}Zn_{3.3}Ge_{40.3}$	14.8	4.2	6.7	74.3	$Ba_8Pd_{2.4}Zn_{3.6}Ge_{40.0}$[b]	1.07664(2)	0.18305(8)	0.1190(1)	0.3110(1)
$Ba_8Cu_2Zn_4Ge_{40}$	14.6	3.9	6.7	74.8	$Ba_8Cu_{2.1}Zn_{3.9}Ge_{40.0}$	1.07318(1)	0.18304(7)	0.1182(1)	0.3116(1)
$Ba_8Cu_3Zn_3Ge_{40}$	14.7	5.8	5.2	74.4	$Ba_8Cu_{3.2}Zn_{2.8}Ge_{40.0}$	1.07185(2)	0.18282(8)	0.1183(1)	0.3124(1)
					$Ba_8Cu_{3.2}Zn_{2.8}Ge_{40.0}$[a]	1.07234(2)	0.18331(8)	0.11834(6)	0.31240(6)
$Ba_8Cu_4Zn_2Ge_{40}$	14.7	7.7	3.4	74.2	$Ba_8Cu_{4.2}Zn_{1.8}Ge_{40.0}$	1.07069(2)	0.18396(1)	0.1190(1)	0.3137(1)
$Ba_8Cu_{5.25}Zn_{0.75}Ge_{40}$	14.7	9.7	1.4	74.2	$Ba_8Cu_{5.2}Zn_{0.8}Ge_{40.0}$	1.06971(1)	0.18242(8)	0.1194(1)	0.3141(1)
$Ba_8Cu_{5.5}Zn_{0.5}Ge_{40}$	14.9	10.0	0.9	74.2	$Ba_8Cu_{5.4}Zn_{0.6}Ge_{40.0}$	1.06922(2)	0.18237(8)	0.11961(8)	0.3149(1)
$Ba_8Cu_{5.75}Zn_{0.25}Ge_{40}$	14.9	10.2	0.7	74.1	$Ba_8Cu_{5.5}Zn_{0.5}Ge_{40.0}$	1.06910(2)	0.18332(7)	0.11973(2)	0.31467(1)
$Ba_8Cu_{5.2}Zn_{0.8}Ge_{40}$	15.1	8.7	2.1	74.1	$Ba_8Cu_{5.2}Zn_{0.8}Ge_{40.0}$[b]	1.06994(2)	0.18322(8)	0.1194(1)	0.3134(1)

Ba sublattice (2*a* and 6*d* sites) was found to be fully occupied.

[a] Lattice parameters and crystallographic data after X-ray single crystal refinement.
[b] Ball milled samples.

samples. X-ray intensity data were recorded from single crystals selected from mechanically crushed alloys with nominal composition $Ba_8Pd_3Zn_3Ge_{40}$ and $Ba_8Cu_3Zn_3Ge_{40}$. In all cases extinctions were consistent with a primitive cubic lattice (space group $Pm\bar{3}n$, $a \sim 1.1$ nm). Ba-atoms, being heavy scatterers, were unambiguously found at the 2*a* and 6*c* site. Constant electron density at the sites 16*i* and 24*k* exclusively reveals Ge occupation in these sites. Metal atoms (Zn, Pd/Cu) randomly share the site 6*d*. A statistical mixture of three species (Zn, Pd/Cu and possible vacancies), however, cannot be elucidated by refinement of X-ray data. In our previous work [1] we have shown that the presence of vacancies in the site 6*d* significantly affects the bonding to the neighboring atoms in the 24*k* site, resulting in split sites $24k_1$ and $24k_2$ [1]. As in the present case no split for the 24*k* site was observed, the 6*d* site was considered as fully occupied by a statistical mixture (Zn:Pd/Cu) where the ratios Zn/Cu and Zn/Pd were fixed from EMPA data (see Tables 2–4b). The vacancy-free crystal structure was also confirmed by structural analysis performed on single crystals selected from the samples with composition at the middle of the solid solutions, e.g., $Ba_8Pd_3Zn_3Ge_{40}$ and $Ba_8Cu_3Zn_3Ge_{40}$. Compositions and crystal structure details for X-ray single crystal and Rietveld refinements are given in Tables 1–4b. As EMPA is not reliable for the estimation of vacancies, the Pd/Zn and Cu/Zn ratios are fixed after EMPA and Rietveld refinements yield a vacancy free crystal structure (accepted compositions in Table 1). The variation of lattice parameters vs. *M*(Pd, Cu) is shown in Fig. 1. It can be seen that lattice parameters for $Ba_8Pd_xZn_yGe_{46-x-y}$ do not show any appreciable change with increase in the Pd content owing to the small difference in the atomic radii of Zn and Pd. On the other hand because of the smaller size of Cu than Zn, shrinkage of the unit cell with increase in the Cu content is observed. Positional parameters vs. *M* content are shown in Figs. 2 and 3.

3.2. Crystal structures of the solid solution $Ba_8Zn_xGe_{46-x-y}Si_y$.

The crystal structure of the solid solution $Ba_8Zn_xGe_{46-x-y}Si_y$ ($y=0$, 8.7, 18.9, 18.2, 27.3; $7.0 \leqslant x \leqslant 7.7$, Table 5) was evaluated by Rietveld refinement of X-ray powder diffraction profiles. In all cases cubic symmetry was confirmed and all measured reflections were indexed in space group $Pm\bar{3}n$. No superstructure reflections indicating a doubling of the unit cell [7] were observed (Fig. 5). The lattice parameters show a linear increase with increase in the Ge content (Fig. 4), a fact, which is in line with the difference of the atomic radii of Ge and Si. The lattice parameters increase by about 3.1% between the end points of the solid solution. In order to elucidate site preferences for Ge/Si substitution the following structural model was used. Ba atoms were placed unambiguously on 2*a* and 6*c* sites and no defect was observed for the 2*a* site [5] for the Si-rich solid solution in contrast to binary $Ba_{8-\delta}Si_{46}$ [8]. Starting with Si distributed on all framework sites (6*d*, 16*i*, 24*k*), refinement of occupation factors for all sites (see Fig. 4) resulted in the following trends for the electron densities with increase in Ge content: (i) an almost linear increase in the 6*d* site, (ii) a linear increase in electron density for the 24*k* site, whilst (iii) a strong negative deviation from linearity was observed for the 16*i* site. Considering such a distribution of electron densities on the one side, interatomic distances (Fig. 4) and atomic radii of the elements on the other side, a model for atom site preference was established which is outlined in Table 6 and Fig. 4.

The small change of the electron density in site 6*d* can be attributed to the Zn/Si substitution. Rietveld refinements for this site reveal a statistical mixture (Si+Zn) for $Ba_8Zn_{7.3}Ge_{10.6}Si_{28.1}$ and $Ba_8Zn_{7.2}Ge_{19.9}Si_{18.9}$, whereas for higher Ge contents the site was fully occupied by Zn (see Table 6 and Fig. 4). The very small difference in X-ray scattering power of Ge and Zn does not allow reliable refinements even with compositional constraints from EPMA data. Therefore, we assume a linear change of the Zn content in the 16*i* and 24*k* sites between occupancies that were established for the end members of the series $Ba_8Zn_7Si_{39}$ [5] and $Ba_8Zn_8Ge_{38}$ [1]. Accordingly only the Ge/Si ratios for the 16*i* and 24*k* sites were refined. These refinements reveal Si/Ge substitutions as shown in

Table 2
X-ray single crystal data for $Ba_8Pd_xZn_{6-x}Ge_{40}$ and $Ba_8Cu_xZn_{6-x}Ge_{40}$ (room temperature, 2Θ range (°) = $2 \leq 2\Theta \leq 72.0$; 50 s/frame, ω-scans, scan width 2°; redundancy > 10); clathrate —type I; space group $Pm\bar{3}n$; no. 223; standardized with program *Structure Tidy* [31]. Anisotropic displacement parameters in 10^2 nm^2.

Parameter/ compound[a]	**$Ba_8Pd_3Zn_3Ge_{40}$**			**$Ba_8Cu_3Zn_3Ge_{40}$**		
Formula from refinement	**$Ba_8Pd_{2.40}Zn_{3.25}Ge_{40.38}$**			**$Ba_8Cu_{3.20}Zn_{2.80}Ge_{40.00}$**		
a [nm]	1.07709(2)			1.07234(2)		
a [nm], Ge standard	1.07683(1)			1.07185(2)		
μ_{abs} [mm^{-1}]	32.16			35.27		
Frames and sets	201, 6 sets			201, 6 sets		
Reflections in refinement	$470 \geq 4\sigma(F_0)$ of 567			$523 \geq 4\sigma(F_0)$ of 567		
Mosaicity	< 0.45			< 0.45		
Variables	17			16		
$R_F^2 = \sum \lvert F_0^2 - F_c^2 \rvert / \sum F_0^2$	0.0245			0.0178		
R_{Int}	0.0376			0.0153		
wR2	0.0534			0.0322		
GOF	1.121			1.158		
Extinction	0.0011(1)			0.0016(1)		
Ba1 in 2a (0,0,0)						
occ.	1.00(1)			1.00(1)		
$U_{11}=U_{22}=U_{33}$	0.0106(2)			0.0096(1)		
Ba2 in 6c (1/4,0,1/2)						
occ.	1.00(1)			1.00(1)		
U_{11}; $U_{22} = U_{33}$	0.0248(4); 0.0537(3)			0.0182(2); 0.0382(2)		
M1 in 6d (1/4,1/2,0)						
occ.[b]	0.54(1)Zn+0.40Pd+0.06Ge			0.53(1)Cu+0.47Zn		
U_{11}; $U_{22} = U_{33}$	0.0143(4); 0.0106(3)			0.0117(3); 0.0097(1)		
Ge2 in 16i (*x*,*x*,*x*)						
x; occ.	0.18327(3); 1.00(1)			0.18331(2); 1.00(1)		
$U_{11}=U_{22}=U_{33}$	0.0099(1)			0.0087(1)		
$U_{23}=U_{13}=U_{12}$	−0.0009(1)			−0.0008(1)		
Ge3 in 24k (0,*y*,*z*)						
y, *z*	0.11859(4); 0.31115(4)			0.11864(2); 0.31240(2)		
occ.	1.00(1)			1.00(1)		
U_{11}; U_{22}	0.0111(2); 0.0126(2)			0.0099(1); 0.0105(1)		
U_{33}; U_{23}	0.0106(2); 0.0009(1)			0.0094(1); 0.0006(1)		
Residual density e$^-$/Å3; max; min	1.67; −1.50			0.92; −0.74		
Principal mean square atomic displacements *U*						
Ba1	0.0106	0.0106	0.0106	0.0096	0.0096	0.0096
Ba2	0.0537	0.0537	0.0248	0.0382	0.0382	0.0182
M1	0.0143	0.0106	0.0106	0.0117	0.0097	0.0097
Ge2	0.0108	0.0108	0.0080	0.0095	0.0095	0.0070
Ge3	0.0129	0.0111	0.0103	0.0108	0.0099	0.0092

Interatomic distances, standard deviation less than 0.0003 nm			
Ba1	−8Ge2	0.3418	0.3403
	−12Ge3	0.3586	0.3582
Ba2	−8Ge3	0.3607	0.3583
	−4M1	0.3807	0.3790
	−8Ge2	0.4005	0.3987
	−4Ge3	0.4160	0.4142
M1	−4Ge3	0.2477	0.2455
	−4Ba2	0.3807	0.3790
Ge2	−1Ge2	0.2489	0.2476
	−3Ge3	0.2505	0.2501
	−1Ba1	0.3418	0.3403
Ge3	−1M1	0.2477	0.2455
	−2Ge2	0.2505	0.2501
	−1Ge3	0.2554	0.2543
	−1Ba1	0.3586	0.3582
	−2Ba2	0.3607	0.3583

[a] Nominal composition.
[b] Pd, Cu, Zn fixed after EMPA.

Table 3a
X-ray powder data for $Ba_8Pd_xZn_{6-x}Ge_{40}$ at $x=0.70$, 0.71, 0.91, 2.40; (room temperature, image plate data collection, Cu $K\alpha_1$ radiation, Θ range $8 \le 2\Theta \le 100$); clathrate type I, space group $Pm\bar{3}n$; no. 223; standardized with program *Structure Tidy* [31].

Parameter/compound[a]	$Ba_8Pd_2Zn_7Ge_{37}$	$Ba_8Pd_1Zn_5Ge_{40}$	$Ba_8Pd_1Zn_5Ge_{40}$	$Ba_8Pd_{2.4}Zn_{3.3}Ge_{40.3}$
Composition, EMPA at.%	$Ba_8Pd_{0.70}Zn_{5.90}Ge_{38.95}$	$Ba_8Pd_{0.71}Zn_{5.66}Ge_{38.64}$	$Ba_8Pd_{0.91}Zn_{5.11}Ge_{39.24}$	$Ba_8Pd_{2.24}Zn_{3.62}Ge_{40.04}\square_{0.08}$
Composition from refinement	$Ba_8Pd_{0.70}Zn_{5.90}Ge_{39.40}$	$Ba_8Pd_{0.71}Zn_{5.66}Ge_{39.63}$	$Ba_8Pd_{0.91}Zn_{5.11}Ge_{39.98}$	$Ba_8Pd_{2.4}Zn_{3.6}Ge_{40.0}$
a (nm), Ge standard	1.07643(1)	1.07632(2)	1.07631(2)	1.07664(2)
Reflections measured	144	144	148	145
Number of variables	24	28	24	17
$R_F=\Sigma\lvert F_o-F_c\rvert/\Sigma F_o$	0.0641	0.0685	0.0714	0.063
$R_I=\Sigma\lvert I_o-I_c\rvert/\Sigma I_o$	0.0836	0.0787	0.0652	0.049
$R_{wP}=[\Sigma w_i\lvert y_{oi}-y_{ci}\rvert^2/\Sigma w_i\lvert y_{oi}\rvert^2]^{1/2}$	0.0875	0.0864	0.0433	0.040
$R_P=\Sigma\lvert y_{oi}-y_{ci}\rvert/\Sigma\lvert y_{oi}\rvert$	0.0557	0.0573	0.0328	0.026
$R_e=[(N-P+C)/\Sigma w_i y_{oi}^2)]^{1/2}$	0.0288	0.0195	0.0297	0.023
$\chi^2=(R_{wp}/R_e)^2$	9.25	19.6	2.12	3.20
Atom parameters				
Ba1 in 2*a* (0, 0, 0); occ.	1.00(1)	1.00(1)	1.00(1)	1.00(1)
B_{iso} (10^2 nm^2)	0.37(6)	0.36(5)	0.32(3)	0.46(5)
Ba2 in 6*c* (1/4,0,1/2); occ.	1.00(1)	1.00(1)	1.00(1)	1.00(1)
B_{iso} (10^2 nm^2)	3.04(6)	2.83(5)	2.75(4)	2.96(6)
***M*1**[b] in 6*d* (1/4, 1/2, 0); occ.	0.12(1)Pd+0.88(1)Zn	0.12(1)Pd+0.88(1)Zn	0.15(1)Pd+0.85(1)Zn	0.38(1)Pd+0.60(1)Zn+0.02(1)Ge
B_{iso} (10^2 nm^2)	0.97(8)	0.70(6)	0.99(4)	0.81(6)
M2 in 16*i* (*x*, *x*, *x*) ; occ.	0.04(1)Zn+0.96(1)Ge	0.02(1)Zn+0.98(1)Ge	1.00(1)Ge	1.00(1)Ge
x	0.18305(9)	0.18335(7)	0.18270(5)	0.18312(8)
B_{iso} (10^2 nm^2)	0.88(4)	0.79(4)	0.98(3)	0.73(4)
Ge3 in 24*k* (0, *y*, *z*); occ.	1.00(1)	1.00(1)	1.00(1)	1.00(1)
y, *z*	0.1181(1); 0.3105(1)	0.1175(1); 0.3103(1)	0.11823(7); 0.31024(7)	0.1189(1); 0.3110(1)
B_{iso} (10^2 nm^2)	0.55(4)	0.52(3)	0.67(2)	0.63(3)
Interatomic distances, standard deviation less than 0.0003 nm				
Ba1–8M2	0.3413	0.3418	0.3406	0.3413
Ba1–12Ge3	0.3576	0.3571	0.3573	0.3583
Ba2–8Ge3	0.3608	0.3607	0.3610	0.3608
Ba2–4*M*1	0.3806	0.3805	0.3805	0.3805
Ba2–8*M*2	0.4005	0.4003	0.4007	0.4004
Ba2–4Ge3	0.4162	0.4168	0.4160	0.4154
*M*1–4Ge3	0.2485	0.2491	0.2487	0.2476
*M*1–4Ba2	0.3806	0.3805	0.3805	0.3805
*M*2–1*M*2	0.2496	0.2485	0.2497	0.2494
*M*2–3Ge3	0.2501	0.2503	0.2509	0.2501
*M*2–1Ba1	0.3413	0.3418	0.3406	0.3413
Ge3–1*M*1	0.2485	0.2491	0.2487	0.2476
Ge3–2*M*2	0.2501	0.2503	0.2509	0.2501
Ge3–1Ge3	0.2542	0.2528	0.2545	0.2559
Ge3–1Ba1	0.3576	0.3571	0.3573	0.3583
Ge3–2Ba2	0.3608	0.3607	0.3610	0.3608
Secondary phase (Ge in vol%)	2.3	–	1.6	1.4

[a] Nominal composition.
[b] Pd, and Zn fix after EMPA.

Table 6, Fig. 4 and the resulting chemical formulae are in good agreement with EPMA for all members of the series. Obviously there is a strong deviation from linearity, particularly for the 16*i* site. In order to prove the reliability of such site preference we performed refinements considering simply a linear change of the atom distribution in these sites (marked by dotted lines Fig. 4). All these models, however, were ruled out by the refinements. The results are in agreement with a study of the ternary solid solution $Ba_{8-\delta}Si_{46-x}Ge_x$ ($0 \le x \le 23$) [8], where at smaller Ge-contents Ge-atoms have a strong preference for the 24*k* site whilst at higher concentration Ge enters the 16*i* site.

Similarly, vacancies in the 6*d* site were not confirmed by Rietveld refinements due to significant disagreement with the resulting formulae and EPMA. All results for Rietveld refinements are shown in Table 6 and Fig. 5. It should be noted, that the refinement of the X-ray powder profile for the sample prepared by ball-milling and hot-pressing yields practically the same results as for the hand-milled and hot-pressed sample with similar composition.

The interatomic distances also increase monotonically with increase in Ge contents in line with the bigger atomic radii of Ge as compared to Si (see Fig. 4). Important interatomic distances are plotted vs. Ge/(Ge+Si) in Fig. 4, where a pronounced effect in case of distances *M*2–*M*2 and *M*3–*M*3 with increase in Ge content is associated with the occupancy factor for the 16*i* and 24*k* site vs. Ge/Si substitution (see Fig. 4). Variation of the free parameters *x* for the site 16*i* (*x*, *x*, *x*) and *y*, *z* for the site 24*k* (0, *y*, z) with increase in Ge content is shown in Fig. 6. The linear increase in the *z* parameter with increase in Ge-content is in line with the difference in atomic radii, $r_{Ge} > r_{Si}$, whereas the *y* parameters simultaneously pass through a maximum.

3.3. Phase equilibria in the quaternary systems Ba–(Pd,Cu)–Zn–Ge and Ba–Zn–Ge–Si

The partial isothermal sections at 800 °C for ternary boundary systems Ba–Zn–Ge and Ba–Pd–Ge were accepted from our recent investigations [1,2] and serve as the basis (i) to construct the quaternary phase diagram for the system Ba–Pd–Zn–Ge at 800 °C and (ii) to define the quaternary single-phase clathrate region $Ba_8Zn_xPd_yGe_{46-x-y-z}\square_z$.

According to Gibbs's phase rule, a four-component system may involve four phases in equilibrium at constant pressure and temperature. The convenient way to present a quaternary equilibrium at constant *P*, *T* is the composition tetrahedron

Table 3b
X-ray powder data for $Ba_8Pd_xZn_{6-x}Ge_{40}$ at $x=1.30$, 1.52, 2.40; (room temperature, image plate data collection, Cu $K_{\alpha1}$ radiation, Θ range $8 \le 2\Theta \le 100$); clathrate type I, space group $Pm\bar{3}n$; no. 223; standardized with program *Structure Tidy* [31].

Parameter/compound[a]	$Ba_8Pd_{2.25}Zn_{3.75}Ge_{40}$	$Ba_8Pd_2Zn_4Ge_{40}$	$Ba_8Pd_3Zn_3Ge_{40}$
Composition, EMPA at.%	$Ba_8Pd_{1.30}Zn_{4.53}Ge_{39.47}$	$Ba_8Pd_{1.52}Zn_{4.41}Ge_{39.19}$	$Ba_8Pd_{2.40}Zn_{3.25}Ge_{40.00}$
Composition from refinement	$Ba_8Pd_{1.30}Zn_{4.53}Ge_{40.17}$	$Ba_8Pd_{1.52}Zn_{4.41}Ge_{40.07}$	$Ba_8Pd_{2.40}Zn_{3.25}Ge_{40.35}$
a (nm), Ge standard	1.07618(1)	1.07680(2)	1.07683(1)
Reflections measured	144	145	143
Number of variables	24	27	24
$R_F=\Sigma\lvert F_o-F_c\rvert/\Sigma F_o$	0.0776	0.0788	0.0734
$R_I=\Sigma\lvert I_o-I_c\rvert/\Sigma I_o$	0.0833	0.0835	0.0683
$R_{wP}=[\Sigma w_i\lvert y_{oi}-y_{ci}\rvert^2/\Sigma w_i\lvert y_{oi}\rvert^2]^{1/2}$	0.0591	0.0562	0.0479
$R_P=\Sigma\lvert y_{oi}-y_{ci}\rvert/\Sigma\lvert y_{oi}\rvert$	0.0449	0.0383	0.0345
$R_e=[(N-P+C)/\Sigma w_i y_{oi}^2)]^{1/2}$	0.0183	0.0202	0.0232
$\chi^2=(R_{wP}/R_e)^2$	10.4	7.70	4.28
Atom parameters			
Ba1 in 2*a* (0,0,0); occ.	1.00(1)	1.00(1)	1.00(1)
B_{iso} (10^2 nm^2)	0.38(5)	0.37(7)	0.36(4)
Ba2 in 6*c* (1/4,0,1/2); occ.	1.00(1)	1.00(1)	1.00(1)
B_{iso} (10^2 nm^2)	3.00(8)	2.65(7)	3.59(4)
***M*1**[b] in 6*d* (1/4,1/2,0); occ.	0.22(1)Pd+0.75(1)Zn+0.03(1)Ge	0.25(1)Pd+0.74(1)Zn+0.01(1)Ge	0.40(1)Pd+0.54(1)Zn+0.06(1)Ge
B_{iso} (10^2 nm^2)	0.77(6)	0.98(7)	0.97(5)
Ge2 in 16*i* (*x*,*x*,*x*); occ.	1.00(1)Ge	1.00(1)Ge	1.00(1)Ge
x	0.1827(1)	0.1833(1)	0.18266(5)
B_{iso} (10^2 nm^2)	0.98(5)	0.84(6)	0.94(5)
Ge3 in 24*k* (0, *y*, *z*); occ.	1.00(1)	1.00(1)	1.00(1)
y, *z*	0.1190(2); 0.3105(2)	0.1184(2); 0.3112(2)	0.11931(8); 0.31137(8)
B_{iso} (10^2 nm^2)	0.72(3)	0.59(4)	0.81(2)
Interatomic distances, standard deviation less than 0.0003 nm			
Ba1–8Ge2	0.3405	0.3419	0.3407
Ba1–12Ge3	0.3578	0.3586	0.3591
Ba2–8Ge3	0.3611	0.3606	0.3609
Ba2–4*M*1	0.3805	0.3807	0.3807
Ba2–8Ge2	0.4006	0.4005	0.4009
Ba2–4Ge3	0.4152	0.4161	0.4152
*M*1–4Ge3	0.2480	0.2478	0.2471
*M*1–4Ba2	0.3805	0.3807	0.3807
Ge2–1Ge2	0.2495	0.2487	0.2501
Ge2–3Ge3	0.2509	0.2506	0.2512
Ge2–1Ba1	0.3405	0.3419	0.3407
Ge3–1*M*1	0.2480	0.2478	0.2471
Ge3–2Ge2	0.2495	0.2506	0.2501
Ge3–1Ge3	0.2561	0.2550	0.2570
Ge3–1Ba1	0.3578	0.3586	0.3591
Ge3–2Ba2	0.3611	0.3606	0.3609
Secondary phase (Ge in vol%)	2.6	–	1.1

[a] Nominal composition.
[b] Pd, and Zn fix after EMPA.

(Roozeboom–Fedorov tetrahedron; simplex). For the correct construction of phase relations among the tie-tetrahedra and adjoining phase fields, the rule of Palatnik and Landau [15] on the association of phase fields may be applied.

The three dimensional phase diagram for the Ba–Pd–Zn–Ge system is shown in Fig. 7a. The connectivity scheme plays a key role to complete the construction of the 3D quaternary phase diagram (Fig. 7d). The general rules for phase field connection in a four-component system imply that two-, three- and four-phase regions are connected to a single-phase body via corresponding surfaces, lines and vertices, respectively. The three phase equilibria κ_1+L+(Ge) (a), $\kappa_1+\tau_2+L$ (b), $\kappa_1+\tau_2+BaGe_2$ (c), $\kappa_1+\tau_1+L$ (e) and $\kappa_1+\tau_1+BaGe_2$ (f) (for a, b, c, e, f see Fig. 7b) involve the κ_1 phase at its maximum solubility for *M* atoms. Therefore, schematic phase equilibria on the basis of the connectivity scheme at 800 °C are presented in Fig. 7b.

The tie-tetrahedron corresponding to the four-phase equilibrium $\kappa_1+\tau_1+\tau_2+L$ appears as simplex "A" in Fig. 7b, which is connected to two three-phase equilibria $\kappa_1+\tau_1+L$ and $\kappa_1+\tau_2+L$ from the ternary boundary systems Ba–Zn–Ge and Ba–Pd–Ge, respectively. The four-phase equilibrium "A" connects to tie-tetrahedron "B" via the three-phase equilibrium $\kappa_1+\tau_1+\tau_2$. The tie-tetrahedron "B" corresponding to the four-phase equilibrium $\kappa_1+\tau_1+\tau_2+BaGe_2$ is derived from two three-phase equilibria $\kappa_1+\tau_1+BaGe_2$ and $\kappa_1+\tau_2+BaGe_2$ in the ternary systems (see connectivity scheme, Fig. 7b and d).

The partial isothermal section "Ba_8Ge_{46}"–"Ba_8Pd_{46}"–"Ba_8Zn_{46}" presented in Fig. 7c lies very close to the phase equilibria $\kappa_1+\tau_1+L$ and $\kappa_1+\tau_2+L$; therefore, the two-phase regions connecting the three-phase equilibria with a single-phase region are very narrow and are not shown in this section. The single-phase region for the clathrate I phase $Ba_8Zn_xPd_y$-$Ge_{46-x-y-z}\square_z$ is outlined in Fig. 7b where the variation of defects can also be seen. The vacancies present in $Ba_8Ge_{43}\square_3$ disappear at $x_{Zn}=6$ in $Ba_8Zn_xGe_{46-x}$ and at $x_{Pd}=4$ in $Ba_8Pd_xGe_{46-x}$. Liquid surfaces extending from two binary systems Pd–Ge and Zn–Ge to the ternary and finally merging in the quaternary system cover a large part of the isothermal section (Fig. 7a).

On the basis of available experimental data on as cast and annealed samples, partial isothermal sections "Ba_8-Ge_{46}"–"Ba_8Cu_{46}"–"Ba_8Zn_{46}" and "Ba_8Ge_{46}"–"Ba_8Si_{46}"–"Ba_8Zn_{46}" at 800 °C are presented in Fig. 8a and b. The single-phase

Table 4a
X-ray powder data for $Ba_8Cu_xZn_{6-x}Ge_{40}$ at $x=2.1$, 3.2, 4.2; (room temperature, image plate data collection, Cu $K\alpha$ radiation, Θ range $8 \le 2\Theta \le 100$); clathrate type I, space group $Pm\bar{3}n$; no. 223); standardized with program *Structure Tidy* [31].

Parameter/compound[a]	**$Ba_8Cu_2Zn_4Ge_{40}$**	**$Ba_8Cu_3Zn_3Ge_{40}$**	**$Ba_8Cu_4Zn_2Ge_{40}$**
Composition, EMPA	**$Ba_8Cu_{2.1}Zn_{3.7}Ge_{40.9}$**	**$Ba_8Cu_{3.2}Zn_{2.8}Ge_{40.6}$**	**$Ba_8Cu_{4.2}Zn_{1.8}Ge_{40.3}$**
Composition from refinement[b]	**$Ba_8Cu_{2.1}Zn_{3.9}Ge_{40.0}$**	**$Ba_8Cu_{3.2}Zn_{2.8}Ge_{40.0}$**	**$Ba_8Cu_{4.2}Zn_{1.8}Ge_{40.0}$**
a (nm), Ge standard	1.07318(1)	1.07185(2)	1.07069(2)
Reflections measured	143	143	143
Number of variables	25	25	25
$R_F=\Sigma\lvert F_o-F_c\rvert/\Sigma F_o$	0.064	0.084	0.087
$R_I=\Sigma\lvert I_o-I_c\rvert/\Sigma I_o$	0.080	0.071	0.072
$R_{wP}=[\Sigma w_i\lvert y_{oi}-y_{ci}\rvert^2/\Sigma w_i\lvert y_{oi}\rvert^2]^{1/2}$	0.077	0.086	0.098
$R_P=\Sigma\lvert y_{oi}-y_{ci}\rvert/\Sigma\lvert y_{oi}\rvert$	0.050	0.061	0.072
$R_e=[(N-P+C)/\Sigma w_i y_{oi}^2)]^{1/2}$	0.021	0.019	0.018
$\chi^2=(R_{wp}/R_e)^2$	13.6	20.5	23.4
Atom parameters			
Ba1 in 2*a* (0, 0, 0); occ.	1.00(1)	1.00(1)	1.00(1)
B_{iso} (10^2 nm^2)	0.50(5)	0.37(5)	0.65(6)
Ba2 in 6*c* (1/4, 0, 1/2); occ.	1.00(1)	1.00(1)	1.00(1)
B_{iso} (10^2 nm^2)	2.47(5)	2.64(5)	2.29(5)
M1[b] in 6*d* (1/4, 1/2, 0); occ.	0.35(1)Cu+0.650Zn	0.53(1)Cu+0.47(1)Zn	0.70(1)Cu+0.30(1)Zn
B_{iso} (10^2 nm^2)	0.45(9)	0.93(8)	0.39(9)
Ge2 in 16*i* (*x*, *x*, *x*); occ.	1.00(1)	1.00(1)	1.00(1)
x	0.18304(7)	0.18282(8)	0.18396(1)
B_{iso} (10^2 nm^2)	0.88(3)	0.91(4)	0.81(4)
Ge3 in 24*k* (0, *y*, *z*); occ.	1.00(1)	1.00(1)	1.00(1)
y, *z*	0.1182(1); 0.3116(1)	0.1183(1); 0.3124(1)	0.1190(1); 0.3137(1)
B_{iso} (10^2 nm^2)	0.86(3)	0.66(3)	0.63(4)
Interatomic distances, standard deviation less than 0.0003 nm			
Ba1–8Ge2	0.3402	0.3394	0.3412
Ba1–12Ge3	0.3576	0.3580	0.3592
Ba2–8Ge3	0.3591	0.3583	0.3573
Ba2–4M1	0.3794	0.3790	0.3785
Ba2–8Ge2	0.3993	0.3990	0.3979
Ba2–4Ge3	0.4150	0.4145	0.4136
M1–4Ge3	0.2468	0.2457	0.2438
M1–4Ba2	0.3794	0.3790	0.3785
Ge2–1Ge2	0.2489	0.2494	0.2449
Ge2–3Ge3	0.2499	0.2499	0.2509
Ge2–1Ba1	0.3402	0.3394	0.3412
Ge3–1M1	0.2468	0.2457	0.2438
Ge3–2Ge2	0.2499	0.2499	0.2509
Ge3–1Ge3	0.2539	0.2537	0.2548
Ge3–1Ba1	0.3576	0.3580	0.3592
Ge3–2Ba2	0.3591	0.3583	0.3573
Secondary phase (Ge in vol%)	1.8	3.3	1.9

[a] Nominal composition.
[b] Cu and Zn fix after EMPA.

region of the clathrate phase is outlined in these sections, which is connected to the corresponding two-phase and three-phase equilibria.

3.4. Physical properties

Transport properties are appropriate to trace the thermoelectric behavior of the clathrates under investigation close to a metal-to-insulator transition. Such a scenario is well documented from both, electrical resistivity and thermopower data.

3.4.1. Electrical resistivity

Fig. 9a shows the temperature dependent electrical resistivity ρ for a set of samples with compositions $Ba_8\{Cu,Pd,Zn\}_xGe_{46-x}$ and $Ba_8Zn_xSi_yGe_{46-x-y}$ and temperatures up to 800 K. The achieved substitution drives a wide span of resistivity data, ranging from a metallic-like behavior in $Ba_8Zn_{7.2}Ge_{19.9}Si_{18.9}$ to a distinctly semiconducting behavior in $Ba_8Cu_{5.2}Zn_{0.8}Ge_{40}$, where the electrical resistivity drops over more than 7 decades from 10 to 800 K. Note that the most pronounced semiconducting behavior is present in the samples with the twofold substituted *d*-elements (Cu/Zn, Pd/Zn), indicating that these materials are near to compensation, i.e., the 16 electrons provided by Ba are fully compensated by holes originated from the Ge/(Cu, Zn, Pd) substitution. (Note for such an estimation that XRSC and XRPD have a detection limit of about 0.2 vacancies per formula unit and uncertainty in EDX data is about 0.5 units per formula unit. Physical property measurements are clearly of higher sensitivity to detect a compensation point of a "Zintl-phase". Moreover, the Zintl count for transition metals is not well defined.) Although the overall view seems to infer such a simple classification, a closer inspection of the data reveals a more complicated temperature dependency, combining metallic and semiconducting features. A qualitative description is then based on the Bloch–Grüneisen formula, which describes the metallic branch of this model, while a simple band model with rectangular bands represents the semiconducting branch. Note that in this model the Fermi energy E_F is located slightly below the appearing band gap, resulting in a distinctly temperature dependent charge carrier density n. The temperature dependent charge carrier density follows in this model by applying the Fermi–Dirac statistics (for more details see, e.g., Ref. [16]). It is interesting to note that the simplified DOS used in the model outlined above (compare also the inset in Fig. 9) fairly well resembles band structure calculations

Table 4b
X-ray powder diffraction data for $Ba_8Cu_xZn_{6-x}Ge_{40}$ at $x=5.2$, 5.4, 5.5; (room temperature, image plate data collection, Cu $K\alpha_1$ radiation, Θ range $8 \le 2\Theta \le 100$); (space group $Pm\bar{3}n$), standardized with program *Structure Tidy* [31].

Parameter/compound[a]	**$Ba_8Cu_{5.25}Zn_{0.75}Ge_{40}$**	**$Ba_8Cu_{5.5}Zn_{0.5}Ge_{40}$**	**$Ba_8Cu_{5.75}Zn_{0.25}Ge_{40}$**	**$Ba_8Cu_{5.2}Zn_{0.8}Ge_{40}$**
Composition, EMPA	**$Ba_8Cu_{5.2}Zn_{0.8}Ge_{40.3}$**	**$Ba_8Cu_{5.4}Zn_{0.5}Ge_{40.0}$**	**$Ba_8Cu_{5.5}Zn_{0.4}Ge_{39.7}$**	**$Ba_8Cu_{4.6}Zn_{1.13}Ge_{39.25}\square_{1.01}$**
Composition from refinement	**$Ba_8Cu_{5.2}Zn_{0.8}Ge_{40.0}$**	**$Ba_8Cu_{5.4}Zn_{0.6}Ge_{40.0}$**	**$Ba_8Cu_{5.5}Zn_{0.5}Ge_{40.0}$**	**$Ba_8Cu_{5.2}Zn_{0.8}Ge_{40}$**
a (nm), Ge standard	1.06971(1)	1.06922(2)	1.06910(2)	1.06994(2)
Reflections measured	144	143	143	143
Number of variables	25	25	25	22
$R_F=\Sigma\lvert F_o-F_c\rvert/\Sigma F_o$	0.059	0.089	0.051	0.067
$R_I=\Sigma\lvert I_o-I_c\rvert/\Sigma I_o$	0.075	0.094	0.056	0.065
$R_{wP}=[\Sigma w_i\lvert y_{oi}-y_{ci}\rvert^2/\Sigma w_i\lvert y_{oi}\rvert^2]^{1/2}$	0.069	0.095	0.089	0.034
$R_P=\Sigma\lvert y_{oi}-y_{ci}\rvert/\Sigma\lvert y_{oi}\rvert$	0.045	0.071	0.062	0.022
$R_e=[(N-P+C)/\Sigma w_i y_{oi}^2)]^{1/2}$	0.029	0.017	0.011	0.020
$\chi^2=(R_{wP}/R_e)^2$	5.62	30.8	64.2	2.86
Atom parameters				
Ba1 in 2*a* (0, 0, 0); occ.	1.00(1)	1.00(1)	1.00(1)	1.00(1)
B_{iso} (10^2 nm^2)	0.46(5)	0.32(5)	0.53(6)	0.63(6)
Ba2 in 6*c* (1/4, 0, 1/2); occ.	1.00(1)	1.00(1)	1.00(1)	1.00(1)
B_{iso} (10^2 nm^2)	2.45(5)	2.64(5)	2.51(5)	2.67(6)
M1[b] in 6*d* (1/4, 1/2, 0); occ.	0.87(1)Cu+0.13(1)Zn	0.90(1)Cu+0.10(1)Zn	0.92(1)Cu+0.08(1)Zn	0.89(1)Cu+0.13(1)Zn
B_{iso} (10^2 nm^2)	0.86(7)	0.92(8)	0.82(7)	1.44(9)
Ge2 in 16*i* (*x*, *x*, *x*) ; occ.	1.00(1)	1.00(1)	1.00(1)	1.00(1)
x	0.18242(8)	0.18237(8)	0.18332(7)	0.18322(8)
B_{iso} (10^2 nm^2)	0.96(4)	0.98(4)	0.60(3)	1.18(4)
Ge3 in 24*k* (0, *y*, *z*); occ.	1.00(1)	1.00(1)	1.00(1)	1.00(1)
y; *z*	0.1194(1); 0.3141(1)	0.11961(8); 0.3149(1)	0.11973(2); 0.31467(1)	0.1194(1); 0.3134(1)
B_{iso} (10^2 nm^2)	0.56(3)	0.40(3)	0.81(3)	0.86(4)
Interatomic distances, standard deviation less than 0.0003 nm				
Ba1–8Ge2	0.3380	0.3377	0.3395	0.3394
Ba1–12Ge3	0.3594	0.3601	0.3599	0.3588
Ba2–8Ge3	0.3569	0.3564	0.3565	0.3573
Ba2–4M1	0.3782	0.3780	0.3780	0.3782
Ba2–8Ge2	0.3984	0.3982	0.3976	0.3979
Ba2–4Ge3	0.4128	0.4126	0.4124	0.4127
M1–4Ge3	0.2430	0.2421	0.2422	0.2436
M1–4Ba2	0.3782	0.3780	0.3780	0.3782
Ge2–1Ge2	0.2504	0.2505	0.2469	0.2474
Ge2–3Ge3	0.2499	0.2502	0.2505	0.2499
Ge2–1Ba1	0.3380	0.3377	0.3395	0.3394
Ge3–1M1	0.2430	0.2421	0.2422	0.2436
Ge3–2Ge2	0.2499	0.2502	0.2505	0.2499
Ge3–1Ge3	0.2555	0.2558	0.2560	0.2555
Ge3–1Ba1	0.3594	0.3601	0.3599	0.3588
Ge3–2Ba2	0.3569	0.3564	0.3565	0.3573
Secondary phase (Ge in vol%)	–	2.9	3.2	1.8

[a] Nominal composition.
[b] Cu and Zn fix after EMPA.

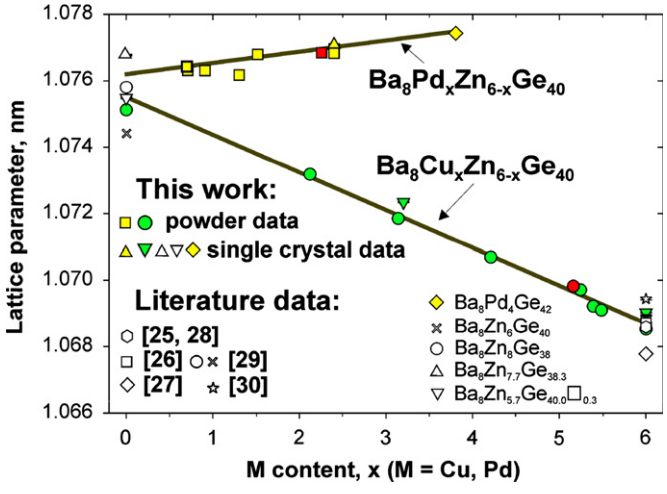

Fig. 1. Lattice parameters vs. *M*-content in $Ba_8M_xZn_{6-x}Ge_{40}$. Data from literature refer to Refs. [25–30].

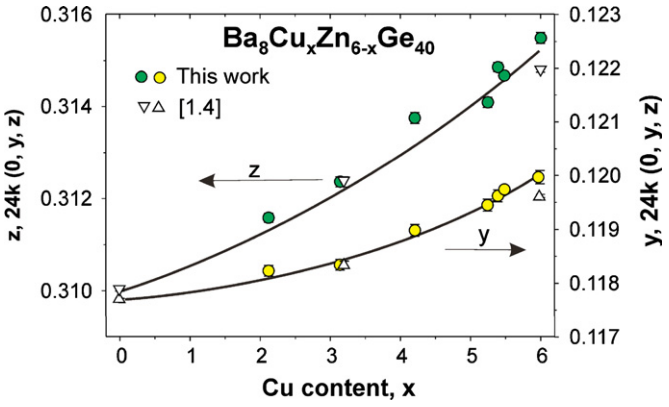

Fig. 2. Atom parameters (*y*, *z*) vs. Cu content in $Ba_8Cu_xZn_{6-x}Ge_{40}$.

performed for $Ba_8M_6Ge_{40}$ [13]. Narrow features of the DOS near to E_F cause additional scattering as noted by Mott and Jones [17]. In the case that this narrow band locates near to a minimum in the density of states, the ρ vs. T curve is expected to exhibit a positive curvature [18]; in fact, this is clearly obvious for $Ba_8Zn_{7.2}Ge_{19.9}Si_{18.9}$ in Fig. 9(b). Although there is substantial variation of the resistivity data, reasonable least squares fits to the model outlined above can be obtained; results are shown as solid lines in Fig. 9(a) and (b). The sketch of the model DOS (inset Fig. 9b) renders schematically DOS features of the ball milled (top) and hand milled (bottom) sample.

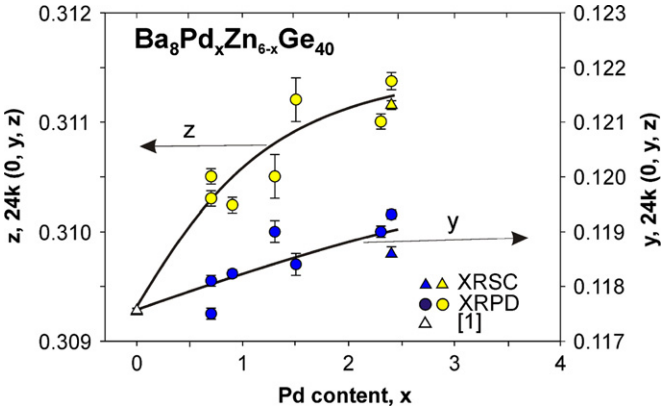

Fig. 3. Atom parameters (y, z) parameters vs. Pd content in $Ba_8Pd_xZn_{6-x}Ge_{40}$.

Comparing $Ba_8Zn_{7.4}Ge_{19.8}Si_{18.8}$ (ball milled) with $Ba_8Zn_{7.2}Ge_{19.9}Si_{18.9}$ (hand milled) reveals significant differences, both with respect to the absolute resistivity values and also with respect to the qualitative temperature dependence. This highlights observations for such materials close to metal-to-insulator states that even the synthesis route might distinctly change physical features.

3.4.2. Thermopower

The temperature dependent thermopower S of $Ba_8\{Cu,Pd,Zn\}_xGe_{46-x}$ and $Ba_8Zn_xSi_yGe_{46-x-y}$ is plotted in Fig. 10(a and b). While the series based on Ge/Si replacements generally reveal almost linearly temperature dependent negative Seebeck coefficients, the systems based on substitution by the transition elements Pd and Cu exhibit a much more complex behavior. The plain data behavior of Fig. 10(a), resulting in negative thermopower values, refers to electrons as the principal charge carriers. A linear temperature dependence of $S(T)$ suggests the absence of any significant electronic correlations in these clathrates; then, $S(T)$ depends primarily on the charge carrier density n. As demonstrated, e.g., in Ref. [19], the diffusion part of the thermopower at higher temperatures can be represented by the simple expression

$$S_d(T > \Theta_D) = \frac{\pi^2 k_B^2 2m}{e\hbar^2(3n\pi^2)^{2/3}}T \quad (1)$$

where m is the effective mass of the charge carriers ($m \sim m_e$) and e is the respective charge. The assumption $m \sim m_e$ is supported by

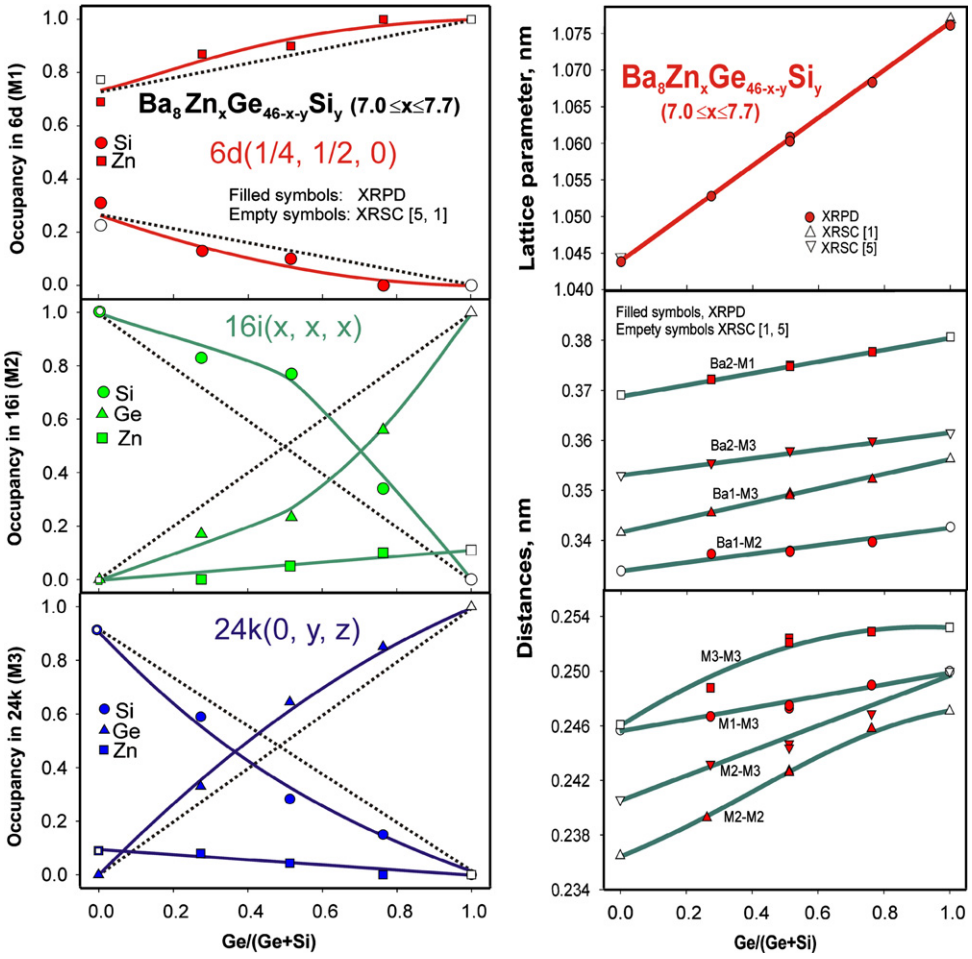

Fig. 4. Lattice parameters, occupancies and interatomic distance vs. Ge/(Ge+Si) in $Ba_8Zn_xGe_{46-x-y}Si_y$ clathrates.

our previous studies [1,2] of the optical conductivity in combination with Hall effect data in Zn and Pd containing Ge-clathrates where $m \sim m_e$. Accordingly, a charge carrier density n can be evaluated, ranging from $n=7.3\times10^{20}$ cm^{-3} in the case of $Ba_8Zn_{7.4}Ge_{19.8}Si_{18.8}$ to $n=2\times10^{21}$ cm^{-3} for $Ba_8Zn_{7.2}Ge_{19.9}Si_{18.9}$. Characteristic for classical high performance thermoelectrics like optimized Bi–Te systems are values of the charge carrier density $n \sim 10^{19}$. The substantial deviation of the thermopower from linearity in the case of $Ba_8Cu_{5.2}Zn_{0.8}Ge_{40.0}$ and $Ba_8Pd_{2.4}Zn_{3.6}Ge_{40.0}$ is accounted for from temperature dependent changes of the energy derivative of the electronic density of states, $N(E)$, at the Fermi level E_F considering Mott's formula

$$S(T) \approx \frac{1}{N(E)}\frac{\delta N(E)}{\delta E}E_F\Big|_{E=E_F} \quad (2)$$

This formula implies that the large $S(T)$ values observed in Fig. 10(b) might be a consequence of steep slopes in a narrow featured DOS around the Fermi level. The dramatic changes with temperature from very large positive to very large negative $S(T)$ values can be conceived from the temperature dependent variation of the Fermi–Dirac (FD) distribution function, which changes a positive slope of $N(E)$ at low temperature to a negative one as a consequence of spectral weight transfer in the FD function to energies beyond E_F for finite temperatures. Note also that the large Seebeck values may be supported by a small overall density of states at the Fermi energy, locating the systems under investigation near to an insulating state. This conclusion perfectly matches the observations made for these two compounds by resistivity measurements.

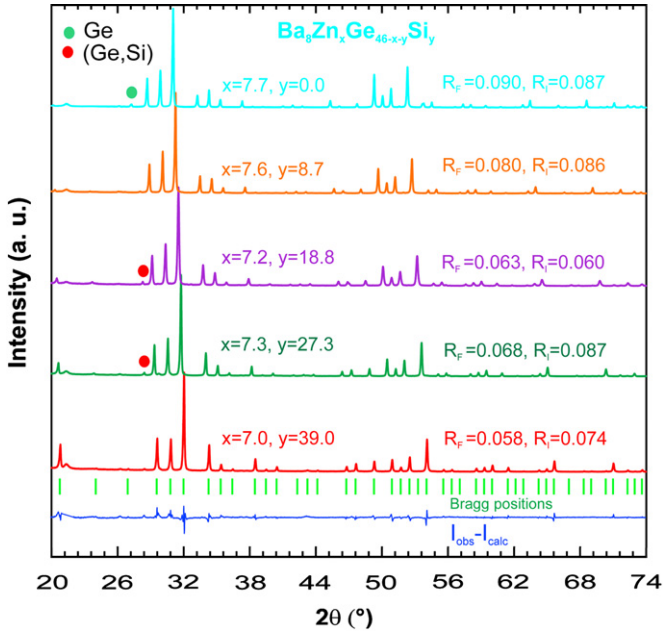

Fig. 5. Comparison of XRPD profiles and Rietveld refinement for $Ba_8Zn_xGe_{46-x-y}Si_y$ clathrates.

3.4.3. Thermal conductivity

The temperature dependent thermal conductivity, λ, of $Ba_8\{Cu,Pd,Zn\}_xGe_{46-x}$ and $Ba_8Zn_xSi_yGe_{46-x-y}$ from 4 to 800 K is summarized in Fig. 11. A more complete set of $\lambda(T)$ data for temperatures below room temperature is presented in Ref. [20]. The experimental data as shown in this figure were obtained from two principally different methods; the standard steady state heat flow method was used below room temperature, while a flash method served above room temperature up to 800 K. Data below room temperature are corrected for their failures due to radiation losses (see later). Overall, thermal conductivity is reasonably small, in favor of thermoelectric applications, and does not exceed a value of 15–20 mW/cm K in the high temperature range. For temperatures above room temperature, $\lambda(T)$ behaves almost constant within the experimental errors. At very low temperatures, some of the data sets exhibit distinctive maxima (e.g., for $Ba_8Zn_{7.2}Ge_{19.9}Si_{18.9}$ or $Ba_8Cu_{5.2}Zn_{0.8}Ge_{40.0}$) as a result of reduced scattering of the heat carrying phonons on static imperfections. Adding the heavy element Pd to these type I clathrates seems to have the strongest impact on a reduction of the thermal conductivity, understandable from the big mass difference between the 3d elements Cu and Zn on the one and Pd on the other hand. Interestingly, the isoelectronic substitution Ge/Si appears to be less influential on $\lambda(T)$. The total thermal conductivity as observed experimentally consists of the lattice (λ_{ph}) and the electronic (λ_e) contribution. Due to the large electrical resistivities observed for both groups of compounds, $\lambda(T)$ is dominated by far by the phonon contribution λ_{ph}. The lattice thermal conductivity λ_{ph} is limited by a variety of scattering processes, which incur the heat carrying phonons. The most relevant ones are scattering on grain boundaries, on defects and impurities, on electrons and by Umklapp processes, accounted for by relaxation times τ_B, τ_D, τ_e and τ_U, respectively. Cage forming compounds like clathrates are famous for resonance scattering yielding an additional reduction of the overall thermal conductivity due to phonon scattering on the loosely bound filler atoms, which create low lying phonon modes [21]. Based on the fact that these individual contributions can be considered independent from each other, the Matthiessen rule applies to derive a total relaxation rate $\tau_c^{-1}=\tau_B^{-1}+\tau_D^{-1}+\tau_e^{-1}+\tau_U^{-1}$. The

Table 5
EPMA and structural data for $Ba_8Zn_xGe_{46-x-y}Si_y$ solid solution.

Nominal composition	EMPA (at%)				EMPA, formula	Accepted composition	Lattice parameter a, nm	Measured relative density (%)
	Ba	Zn	Ge	Si				
$Ba_8Zn_8Ge_{10}Si_{28}$	15.28	14.0	20.8	49.9	$Ba_8Zn_{7.3}Ge_{11.4}Si_{27.3}$	$Ba_8Zn_{7.3}Ge_{10.6}Si_{28.1}$	1.05278(2)	86.6
$Ba_8Zn_8Ge_{19}Si_{19}$	14.8	13.6	36.6	35	$Ba_8Zn_{7.4}Ge_{19.7}Si_{18.9}$	$Ba_8Zn_{7.4}Ge_{19.8}Si_{18.8}$	1.06086(2)	92.0
$Ba_8Zn_8Ge_{19}Si_{19}$	15.0	13.5	38.0	33.5	$Ba_8Zn_{7.2}Ge_{20.6}Si_{18.2}$	$Ba_8Zn_{7.2}Ge_{19.9}Si_{18.9}$	1.06026(2)	91.8
$Ba_8Zn_8Ge_{28}Si_{10}$	14.7	14.1	55.0	16.2	$Ba_8Zn_{7.6}Ge_{29.7}Si_{8.7}$	$Ba_8Zn_{7.6}Ge_{29.3}Si_{9.1}$	1.06833(2)	88.1
$Ba_8Zn_8Si_{38}$	–	–	–			$Ba_8Zn_7Si_{39}$	1.04382(2) [5]	–
$Ba_8Zn_8Ge_{38}$	–	–	–			$Ba_8Zn_{7.7}Si_{38}$	1.07647(3) [1]	–
$Ba_8Cu_{5.2}Zn_{0.8}Ge_{40}$	15.09	8.70	2.13	74.06	–	$Ba_8Cu_{5.2}Zn_{0.8}Ge_{40.0}$	1.06994(2)	96.9
$Ba_8Pd_{2.4}Zn_{3.3}Ge_{40.3}$	14.84	4.17	6.72	74.27	–	$Ba_8Pd_{2.3}Zn_{3.6}Ge_{40.1}$	1.07664(2)	97.6

Table 6
X-ray powder diffraction data for $Ba_8Zn_xGe_{46-x-y}Si_y$ solid solution (room temperature, image plate data collection, Cu $K_{\alpha 1}$ radiation, Θ range $8 \le 2\Theta \le 100$); (space group $Pm\bar{3}n$), standardized with program *Structure Tidy* [31].

Parameter/compound[a]	$Ba_8Zn_8Ge_9Si_{29}$	$Ba_8Zn_8Ge_{19}Si_{19}$	$Ba_8Zn_8Ge_{29}Si_9$
Composition, EMPA	$Ba_8Zn_{7.3}Ge_{11.4}Si_{27.3}$	$Ba_8Zn_{7.2}Ge_{20.6}Si_{18.2}$	$Ba_8Zn_{7.6}Ge_{29.7}Si_{8.7}$
Composition from refinement[b]	$Ba_8Zn_{7.3}Ge_{10.6}Si_{28.1}$	$Ba_8Zn_{7.2}Ge_{19.9}Si_{18.9}$	$Ba_8Zn_{7.4}Ge_{29.3}Si_{9.1}$
a [nm], Ge standard	1.05278(2)	1.06026(2)	1.06833(2)
Reflections measured	135	143	145
Number of variables	22	22	20
$R_F=\Sigma\lvert F_o-F_c\rvert/\Sigma F_o$	0.066	0.066	0.080
$R_I=\Sigma\lvert I_o-I_c\rvert/\Sigma I_o$	0.085	0.061	0.086
$R_{wP}=[\Sigma w_i\lvert y_{oi}-y_{ci}\rvert^2/\Sigma w_i\lvert y_{oi}\rvert^2]^{1/2}$	0.066	0.028	0.051
$R_P=\Sigma\lvert y_{oi}-y_{ci}\rvert/\Sigma\lvert y_{oi}\rvert$	0.043	0.020	0.038
$R_e=[(N-P+C)/\Sigma w_i y_{oi}^2)]^{1/2}$	0.026	0.023	0.030
$\chi^2=(R_{wp}/R_e)^2$	6.22	1.46	2.83
Atom parameters			
Ba1 in 2*a* (0, 0, 0); occ.	1.0(1)	1.0(1)	1.0(1)
B_{iso} (10^2 nm^2)	0.71(6)	0.97(5)	1.11(6)
Ba2 in 6*c* (1/4, 0, 1/2); occ.	1.0(1)	1.0(1)	1.00(1)
B_{iso} (10^2 nm^2)	2.33(5)	2.88(5)	3.32(6)
M1 in 6*d* (1/4, 1/2, 0); occ.	0.87(1)Zn+0.13(1)Si	0.90(1)Zn+0.10(1)Si	1.0(1)Zn
B_{iso} (10^2 nm^2)	0.86(8)	0.50(6)	1.30(8)
M2 in 16*i* (*x*, *x*, *x*); occ.	0.83(1)Si+0.17(1)Ge	0.77(1)Si+0.23(1)Ge+0.05(1)Zn[c]	0.34(1)Si+0.56(1)Ge+0.1(1)Zn
x	0.1844(2)	0.18421(9)	0.1836(1)
B_{iso} (10^2 nm^2)	1.26(8)	1.22(5)	1.60(6)
M3 in 24*k* (0, *y*, *z*); occ.	0.59(1)Si+0.338(1)Ge+0.08Zn	0.27(1)Si+0.64(1)Ge+0.04(1)Zn[c]	0.15(1)Si+0.85(1)Ge
y; *z*	0.1183(2); 0.3061(2)	0.1187(1); 0.3069(1)	0.1184(1); 0.3077(1)
B_{iso} (10^2 nm^2)	0.75(5)	1.02(4)	1.19(4)
Interatomic distances, standard deviation <0.0003 nm			
Ba1–8M2	0.3373	0.3381	0.3397
Ba1–12M3	0.3455	0.3487	0.3522
Ba2–8M3	0.3555	0.3576	0.3599
Ba2–4M1	0.3722	0.3747	0.3777
Ba2–8M2	0.3906	0.3937	0.3972
Ba2–4M3	0.4063	0.4085	0.4123
M1–4M3	0.2467	0.2475	0.2490
M1–4Ba2	0.3722	0.3747	0.3777
M2–1M2	0.2392	0.2415	0.2458
M2–3M3	0.2432	0.2446	0.2469
M2–1Ba1	0.3734	0.3381	0.3379
M3–2M2	0.2432	0.2446	0.2469
M3–1M1	0.2467	0.2475	0.2490
M3–1M3	0.2488	0.2516	0.2529
M3–1Ba1	0.3455	0.3487	0.3522
M3–2Ba2	0.3551	0.3576	0.3599
Secondary Phase (Ge,Si, vol%)	1.4	None	None

[a] Nominal composition.
[b] Accepted composition.
[c] Zn fixed considering linear increase or decrease with Ge content.

temperature dependence of λ_{ph} follows from the basic thermodynamic expression $\lambda=(1/3)C_V v l$, where C_V is the heat capacity of the system, v the particle velocity and l the mean free path. Callaway and von Baeyer [22] demonstrated that this transforms for the heat carrying lattice vibrations to

$$\lambda_{ph}=\frac{k_B}{2\pi^2\upsilon_s}\left(\frac{k_B}{\hbar}\right)^3 T^3\int_0^{\theta_D/T}\frac{\tau_c x^4 e^x}{(e^x-1)^2}\,dx$$
$$\upsilon_s=\frac{k_B\theta_D}{\hbar(6\pi^2 N)^{1/3}}\quad\text{and}\quad x=\frac{\hbar\omega}{k_B T} \tag{3}$$

with υ_s the velocity of sound calculated in terms of the Debye model, N is the number of atoms per unit volume and ω the phonon frequency. In the case of reasonably pure systems an additional term in Eq. (3) has to be taken into account, which, however, for the high resistance materials studied here can be neglected [23]. Assuming the applicability of the Wiedemann Franz law with $L_0=2.45\times10^{-8}\,\mathrm{W\,\Omega\,K^{-2}}$, the phonon conductivity was obtained by subtracting the electronic part $\lambda_e(T)=L_0T/\rho(T)$ from the total measured thermal conductivities and accounting for the radiation losses via a T^3 term.

Fig. 12 shows the low temperature part of the thermal conductivity of $Ba_8Zn_{7.3}Ge_{10.6}Si_{28.1}$. Summarized are the total thermal conductivity λ, the electronic part λ_e and the phonon part λ_{ph}. The application of the Wiedemann–Franz law evidences that λ_e, is, in fact, negligible. The room temperature resistivity of $Ba_8Zn_{7.3}Ge_{10.6}Si_{28.1}$ is about 12800 μ Ω cm; thus, λ_e ~0.6 mW/cm K, much smaller than the overall experimentally derived values. The contribution regarding the radiation loss is indicated, too. Using the steady state heat flux measurement method causes significant losses at high temperatures, comparable to the overall measured data, specifically in those cases where $\lambda(T)$ is small. In comparison to other alloys of this study, $\lambda(T)$ of $Ba_8Zn_{7.3}Ge_{10.6}Si_{28.1}$ does not exhibit a pronounced low temperature maximum as frequently observed in both cases, if either the lattice part dominates or the electronic one. The disappearance of such a pronounced maximum in the former case results from enhanced scattering of phonons on defects and grain boundaries, represented by τ_D and τ_b, respectively. Interplay of weak defect

and boundary scattering with Umklapp processes would then be responsible for establishing the low temperature maximum in $\lambda(T)$ as it is the case, e.g., for $Ba_8Cu_{5.2}Zn_{0.8}Ge_{40}$. The least squares fit of Eq. (3) to the experimental data of Fig. 12 reveals the Debye temperature $\theta_D \sim 200$ K. Note that a much better fit would be possible, if unphysical low θ_D values would be permitted. Eq. (3) also demonstrates that the position of the maximum of $\lambda(T)$ at low temperatures weakly depends on the Debye temperature. In order to face the observed thermal conductivity data with the theoretical lower limit λ_{min}, i.e., if scattering would happen at each lattice site, the model of Cahill and Pohl [24] is used, allowing to compute $\lambda_{min}(T)$ from the number of atoms per unit volume and from the Debye temperature θ_D. Taking $N = 4.74 \times 10^{28}$ m^{-3} and $\theta_D = 200$ K reveals $\lambda_{min}(300\text{ K}) \sim 4$ mW/cm K (shaded area, Fig. 12). Data derived from this model are well below the experimentally accessed figures.

To classify clathrates with respect to thermoelectric applications, the ZT values of $Ba_8\{Cu,Pd,Zn\}_xGe_{46-x}$ and $Ba_8Zn_xSi_yGe_{46-x-y}$ are computed from $ZT = TS^2/(\rho\lambda)$ using the experimental data collected for S, ρ and λ (see Fig. 13(a and b)).

Among the materials investigated in this study, $Ba_8Zn_{7.4}Ge_{19.8}Si_{18.8}$ exhibits the largest ZT value, reaching about 0.45 at 765 K with a tendency to still higher values at more elevated temperatures. While for the materials studied there are no distinct differences of $\lambda(T)$ at higher temperatures, pronounced differences in the electrical resistivity are decisive for a high figure of merit, although the respective Seebeck coefficient may not be the highest. In general, $ZT(T)$ are smoothly varying curves; ZT of $Ba_8Cu_{5.2}Zn_{0.8}Ge_{40}$, however, interestingly shows three transitions through zero points as a result of the various crossovers from positive to negative Seebeck coefficients (Fig. 13(b)). Although the differences in the thermoelectric properties among our quaternary and ternary Cu-, Zn- Pd-containing Ge-based clathrate series are not significant, the ZT-values of Ge/Si substituted Zn clathrates ($ZT = 0.45$ at 800 K) are particularly encouraging with respect to the replacement of expensive Ge by low-price elements (Zn, Si).

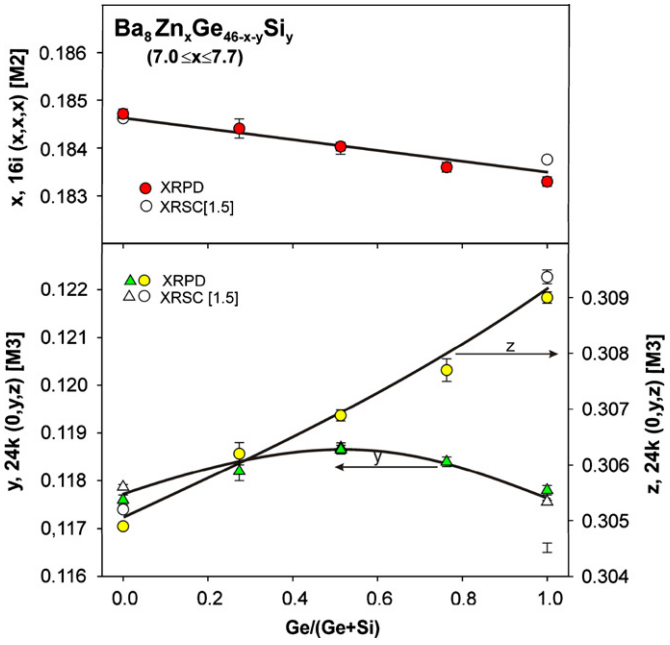

Fig. 6. Atom parameters vs. Ge/(Ge+Si) in $Ba_8Zn_xGe_{46-x-y}Si_y$ clathrates.

4. Conclusion

Vacancy-free quaternary clathrate solid solutions $Ba_8Zn_xGe_{46-x-y}Si_y$, $Ba_8(Zn,Cu)_xGe_{46-x}$ and $Ba_8(Zn,Pd)_xGe_{46-x}$ were prepared and characterized by X-ray powder diffraction, X-ray single crystal diffraction, EMPA. All compounds crystallize in

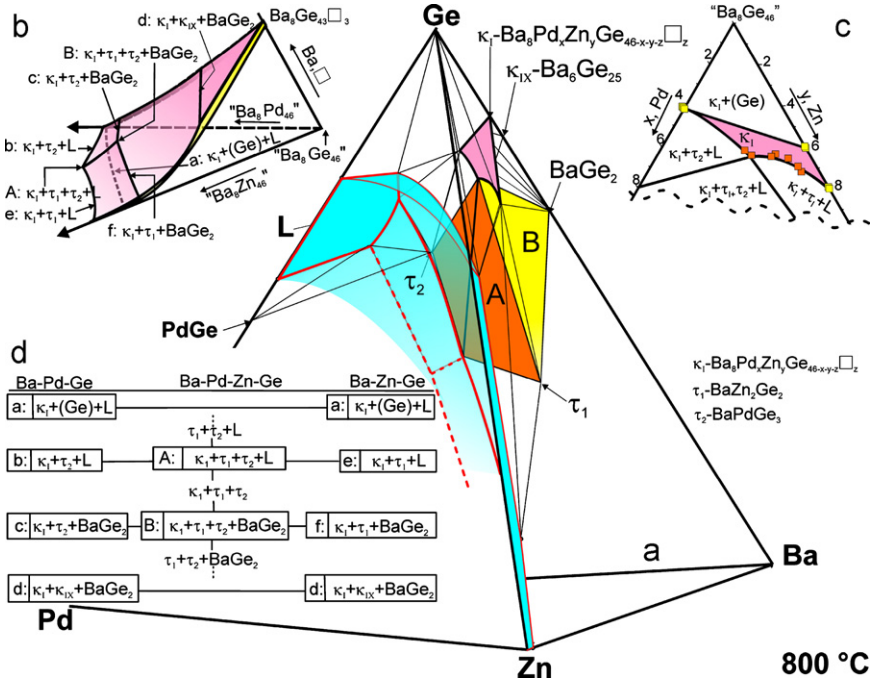

Fig. 7. Ba–Pd–Zn–Ge system at 800 °C: (a) three dimensional view of quaternary phase diagram; (b) schematic phase equilibria; (c) partial isothermal section "Ba_8Ge_{46}"–"Ba_8Pd_{46}"–"Ba_8Zn_{46}"; (d) connectivity scheme.

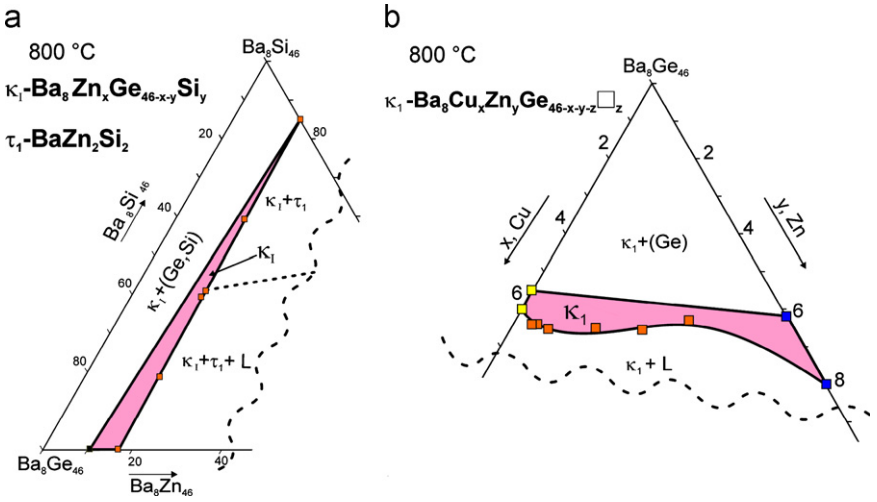

Fig. 8. Partial isothermal section at 800 °C: (a) "Ba_8Ge_{46}"–"Ba_8Si_{46}"–"Ba_8Zn_{46}"; (b) "Ba_8Ge_{46}"–"Ba_8Cu_{46}"–"Ba_8Zn_{46}".

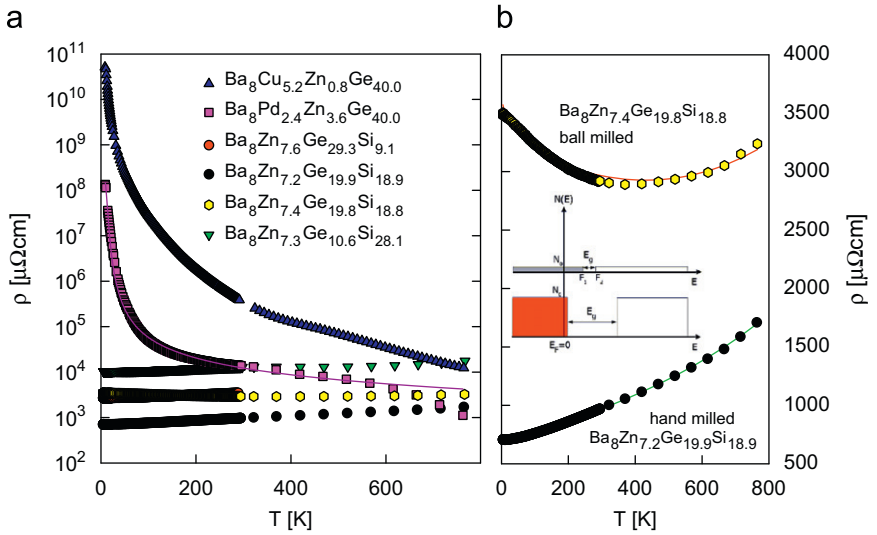

Fig. 9. (a) Temperature dependent electrical resistivity ρ of various concentrations of $Ba_8\{Cu,Pd,Zn\}_xGe_{46-x}$ and $Ba_8Zn_xSi_yGe_{46-x-y}$ plotted on a logarithmic resistivity axis. (b) Resistivity details for $Ba_8Zn_{7.4}Ge_{19.8}Si_{18.8}$ (ball milled) and $Ba_8Zn_{7.2}Ge_{19.9}Si_{18.9}$ (hand milled). The solid lines in both panels are least squares fits as explained in the text. The insert in panel (b) sketches a simplified electronic density of states around the Fermi energy. The upper part refers to the ball milled and the lower part to the hand milled compound.

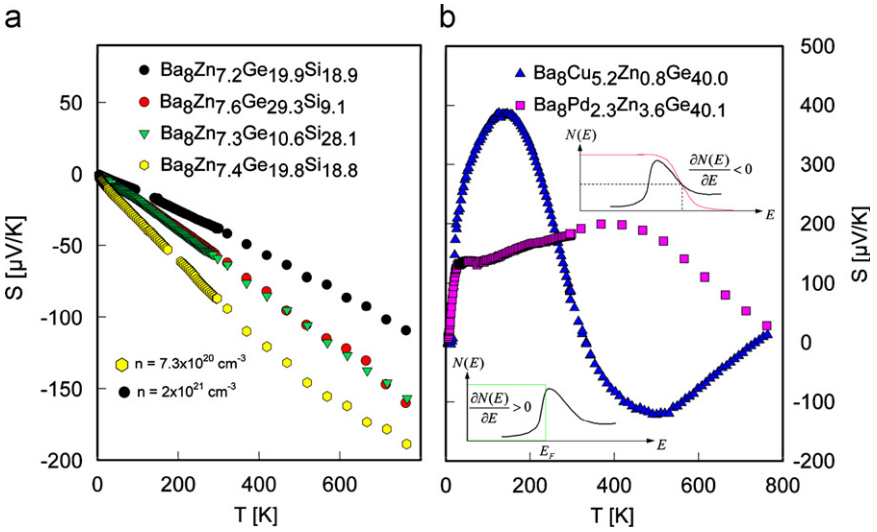

Fig. 10. Temperature dependent thermopower S for various concentrations of $Ba_8Zn_xSi_yGe_{46-x-y}$ (a), $Ba_8Zn_{0.8}Cu_{5.2}Ge_{46-x}$, and $Ba_8Zn_{3.6}Pd_{2.3}Ge_{46-x}$ (b) from 4 to 800 K. The insets in panel (b) schematically represent density of state features near the Fermi energy together with the Fermi Dirac distribution function for $T=0$ and >0 to explain the temperature dependent thermopower.

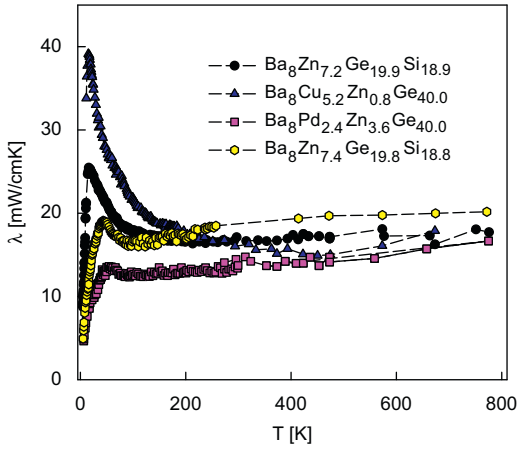

Fig. 11. Temperature dependent thermal conductivity λ of $Ba_8\{Cu,Pd,Zn\}_xGe_{46-x}$ and $Ba_8Zn_xSi_yGe_{46-x-y}$ for temperatures up to 800 K.

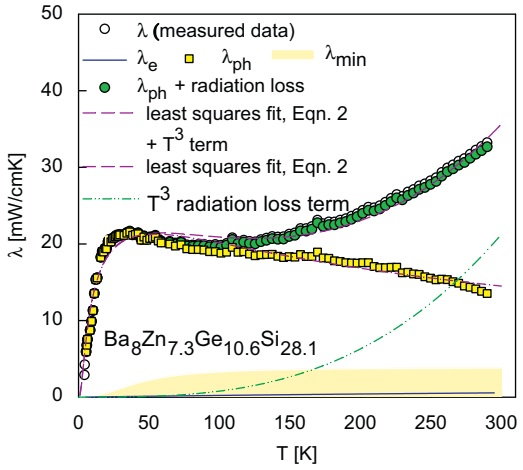

Fig. 12. Temperature dependent thermal conductivity λ of $Ba_8Zn_{7.3}Ge_{10.6}Si_{28.1}$ for temperatures up to 300 K. λ_e is determined by the Wiedemann Franz law and $\lambda_{ph}=\lambda-\lambda_e$. Least squares fits are based on Eq. (3) and λ_e is determined by the model of Cahill and Pohl [24].

space group $Pm\bar{3}n$, isotypic with clathrate type I. Site preference for each case was evaluated. *M* atoms (Zn, Pd, Cu) in $Ba_8(Zn, Cu)_xGe_{46-x}$, $Ba_8(Zn, Pd)_xGe_{46-x}$ randomly share the site 6*d*. Linear substitution of Zn at the 6*d* site in the $Ba_8Zn_xGe_{46-x-y}Si_y$ solid solution was observed. Lattice parameters show a linear increase with increase in Ge for the $Ba_8Zn_xGe_{46-x-y}Si_y$ solid solution.

Isothermal section at 800 °C for the quaternary system Ba–Pd–Zn–Ge was constructed and partial isothermal sections Ba_8Ge_{46}–Ba_8Pd_{46}–Ba_8Zn_{46}, Ba_8Ge_{46}–Ba_8Cu_{46}–Ba_8Zn_{46} and Ba_8Ge_{46}–Ba_8Si_{46}–Ba_8Zn_{46} at 800 °C are presented.

Electronic and thermal transport in the temperature range from 4.2 to 800 K characterize the materials investigated to be located near to a metal to insulator transition. The latter is unambiguously obvious from a resistivity with negative temperature coefficient varying over more than 6 orders of magnitude ($Ba_8Cu_{5.2}Zn_{0.8}Ge_{40.0}$) to a metallic-like behavior observed for $Ba_8Zn_{7.2}Ge_{19.9}Si_{18.9}$. Concomitantly, very large Seebeck coefficients are found for the almost insulating phases $Ba_8Cu_{5.2}Zn_{0.8}Ge_{40.0}$ and $Ba_8Pd_{2.4}Zn_{3.6}Ge_{40.0}$, where narrow features in the electronic DOS with considerable small absolute values give rise to a strong temperature variation reaching giant Seebeck values of about 400 μV/K even at temperatures of about 150 K. A simple Zintl count reveals slight electron deficiencies for $Ba_8Cu_{5.2}Zn_{0.8}Ge_{40.0}$ and $Ba_8Pd_{2.4}Zn_{3.6}Ge_{40.0}$, whereas the remaining compounds have excess in electrons, both scenarios are in line with the transport data observed. Even subtle differences in the electron balance derived from the Zintl model are well reflected from the absolute resistivity values. The *ZT* values achieved are already in a promising order of magnitude particularly for those compositions where costly germanium was substituted by inexpensive silicon ($ZT=0.45$ at 800 K for $Ba_8Zn_{7.4}Ge_{19.8}Si_{18.8}$).

Acknowledgments

The research reported herein was supported by the Higher Education Commission of Pakistan (HEC) under the scholarship scheme Ph.D. in Natural & Basic Sciences from Austria. We are grateful for financial support by the Austrian FFG, Project "THECLA".

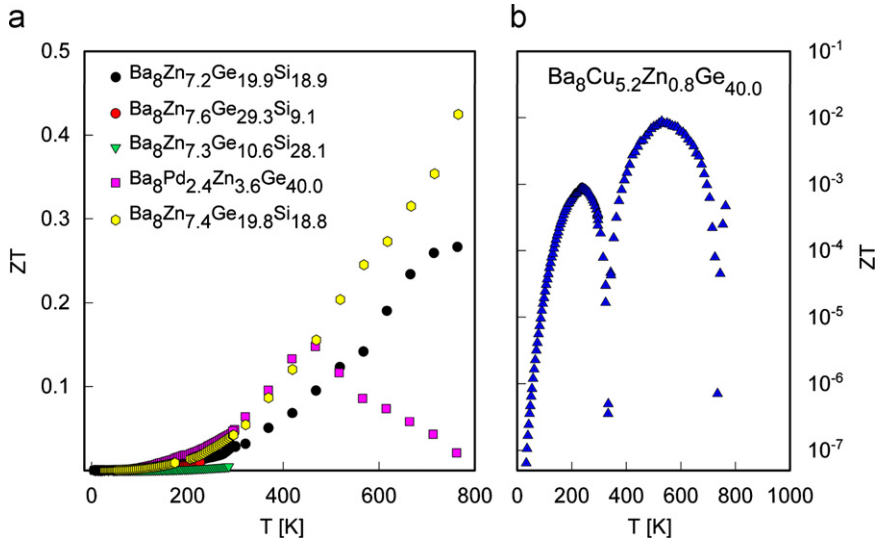

Fig. 13. (a) Temperature dependent figure of merit *ZT* of $Ba_8\{Cu,Pd,Zn\}_xGe_{46-x}$ and $Ba_8Zn_xSi_yGe_{46-x-y}$. (b) *ZT*(*T*) of $Ba_8Cu_{5.2}Zn_{0.8}Ge_{40.0}$ on a logarithmic *ZT* scale. Quaternary phase diagram of Ba–Pd–Zn–Ge system at 800 °C.

References

[1] N. Melnychenko-Koblyuk, A. Grytsiv, L. Fornasari, H. Kaldarar, H. Michor, F. Röhrbacher, M. Koza, E. Royanian, E. Bauer, P. Rogl, M. Rotter, H. Schmid, F. Marabelli, A. Devishvili, M. Doerr, G. Giester, J. Phys.: Condens. Matter 19 (2007) 216223.

[2] N. Melnychenko-Koblyuk, A. Grytsiv, P. Rogl, M. Rotter, E. Bauer, G. Durand, H. Kaldarar, R. Lackner, H. Michor, E. Royanian, M. Koza, G. Giester, Phys. Rev. B 76 (2007) 144118.

[3] N. Melnychenko-Koblyuk, A. Grytsiv, St. Berger, H. Kaldarar, H. Michor, F. Röhrbacher, E. Royanian, E. Bauer, P. Rogl, H. Schmid, G. Giester, J. Phys. Condens. Matter 19 (2007) 046203.

[4] N. Melnychenko-Koblyuk, A. Grytsiv, P. Rogl, H. Schmid, G. Giester, J. Solid State Chem. 182 (2009) 1754.

[5] N. Nasir, A. Grytsiv, N. Melnychenko-Koblyuk, P. Rogl, E. Bauer, R. Lackner, E. Royanian, G. Giester, A. Saccone, J. Phys.: Condens. Matter 21 (2009) 385404.

[6] A. Grytsiv, N. Melnychenko-Koblyuk, N. Nasir, P. Rogl, A. Saccone, H. Schmid, Int. J. Mater. Res. (Z. Metallkd.) 100 (2009) 189.

[7] W. Carrrillo-Cabrera, S. Budnyk, Y. Prots, Y. Grin, Z. Anorg. Allg. Chem. 630 (2004) 7226.

[8] H. Fukuoka, J. Kiyoto, S. Yamanaka, J. Solid State Chem. 175 (2003) 237–244.

[9] K. Suekuni, M.A. Avila, K. Umeo, T. Takabatake, Phys. Rev. B 75 (2007) 195210.

[10] J. Martin, S. Erickson, G.S. Nolas, P. Alboni, T.M. Tritt, J. Yang, J. Appl. Phys. 99 (2006) 044903.

[11] E.N. Nenghabi, C.W. Myles, Phys. Rev. B 77 (2008) 205203.

[12] A. Saramat, G. Svensson, A.E.C. Palmqvist, C. Stiewe, E. Mueller, D. Platzek, S.G.K. Williams, D.M. Rowe, J.D. Bryan, G.D. Stucky, J. Appl. Phys. 99 (2006) 23708-1.

[13] S. Johnsen, A. Bentien, G.K.H. Madsen, M. Nygren, B.B. Iversen, Phys. Rev. B 76 (2007) 245126.

[14] Pauling File Binaries Edition, release 2002/1 Version 1.0, ASM Intl., Materials Park, OH, USA.

[15] L.S. Palatnik , A.I. Landau, 1961, Phase Equilibria in Multi-Component Systems, Holt, Rinehart & Winston Inc., NewYork, Chicago, San Francisco, Toronto, London, pp. 270–320 (translated from Kharkov State University Press, 1964).

[16] St. Berger, Ph.D. Thesis, Vienna University of Technology, Vienna, Austria, 2003.

[17] N.F. Mott, H. Jones, in: Theory of the Properties of Metals and Alloys, Dover, New York, 1936.

[18] J.C. Chiu H, Phys. Rev. B 13 (1976) 1507.

[19] F.J. Blatt, in: Physics of Electronic Conduction in Solids, McGraw Hill, New York, 1968, pp. 210.

[20] I. Bednar, G. Csaszar, M. Menhart, S. Bühler-Paschen, E. Bauer, N. Nasir, A. Grytsiv, N. Melnychenko-Koblyuk, P. Rogl, ICT, Freiburg, Germany, 2009.

[21] J.L. Cohn, G.S. Nolas, V. Fessatidis, T.H. Metcalf, G.A. Slack, Phys. Rev. Lett. 82 (1999) 779.

[22] J. Callaway, H.C. von Baeyer, Phys. Rev. 120 (1960) 1149.

[23] J. Yang, in: T.M. Tritt (Ed.), Thermal Conductivity, Theory, Properties and Applications, Springer, 2004, pp. 1.

[24] D. Cahill, R. Pohl, Solid State Commun. 70 (1989) 927.

[25] G. Cordier, P. Woll, J. Less Common. Metal. 169 (1991) 291.

[26] L. Yang, Ji-Chi, G. Weiping, S. Khandekar, J.H. Ross, J. Phys.: Condens. Mater. 15 (2003) 5535.

[27] L. Yang, Y. Wang, T. Liu, T.D. Hu, B.X. Li, K. Stahl, S.Y. Chen, M.Y. Li, P. Shen, G.L. Lu, Y.W. Wang, J.Z. Jiang, J. Solid State Chem. 178 (2005) 1773.

[28] M. Hokazono, H. Anno, K. Matsubara, Mater. Trans. 46 (2005) 1485.

[29] B. Kuhl, A. Czybulka, H.U. Schuster, Z. Anorg. Allg. Chem. 621 (1995) 1.

[30] S. Johnsen, A. Bentien, G.K.H. Madsen, M. Nygren, B.B. Iversen, in: Proceedings of the 24th International Conference on Thermoelectrics ICT IEEE Cat. No. 05TH8854C, 2005, pp. 226.

[31] E. Parthé, L. Gelato, B. Chabot, M. Penzo, K. Cenzual, R. Gladyshevskii, in: TYPIX—Standardized Data and Crystal Chemical Characterization of Inorganic Structure Types, Springer-Verlag, Berlin, Heidelberg, 1994.